Chemically produced tungsten–praseodymium oxide composite sintered by spark plasma sintering

Xiao-Yu Ding [a], Lai-Ma Luo [a,c,*], Ze-Long Lu [a], Guang-Nan Luo [b], Xiao-Yong Zhu [a,c], Ji-Gui Cheng [a,c], Yu-Cheng Wu [a,c,*]

[a] School of Materials Science and Engineering, Hefei University of Technology, Hefei 230009, China
[b] Institute of Plasma Physics, Chinese Academy of Sciences, Hefei 230031, China
[c] Engineering Research Center of Powder Metallurgy of Anhui Province, Hefei 230009, China

HIGHLIGHTS

- Wet chemical method was used to prepare highly uniform Pr_2O_3 doped $W–Pr_2O_3$ powder.
- The Pr_2O_3 particles significantly refine the grain size of tungsten alloy.
- The tensile strength of Pr_2O_3/W samples were higher than those of pure W samples.

ARTICLE INFO

ABSTRACT

Pr_2O_3 doped W composite were synthesized by a novel wet chemical method and spark plasma sintering. The grain size, relative density and the Vicker hardness $HV_{0.2}$ of Pr_2O_3/W samples were 4 μm, 98.3% and 377.2, respectively. The tensile strength values of Pr_2O_3/W were higher than those of pure W. As the temperature rises from 25 °C to 800 °C, the conductivity of pure W and $W–1$ wt% Pr_2O_3 composites decreased with the same trend, was above 150 W/m K.

1. Introduction

As a refractory metal with the highest melting point (3440 °C), tungsten is supposed to be the most promising candidate for plasma facing first wall material in future fusion reactors due to its superiority to other materials in many respects, including good thermal conductivity, low thermal expansion coefficient, high moduli of elasticity, good thermal shock resistances, high strength at elevated temperatures, low sputtering yield, high sputtering resistance and low tritium inventory [1–8]. Tungsten materials, however, are facing serious challenge of brittleness in different aspects i.e. low-temperature brittleness, recrystallization brittleness and radiation induced brittleness [9–13]. Second-phase particles (La_2O_3, Y_2O_3, TiC, HfC, Ta_2C, TiN, etc.) [14–16] dispersoids can play a major role in mitigating these problems. Rare-earth oxide particles are particularly effective, because they can gather solutes owing to strong rare-earth–oxygen interactions. They can refine the grains by promoting grain nucleation and hindering grain growth. The refined microstructure will result in not only a significant increase in strength, but also abundant grain boundary areas that can depress the concentration of deleterious solutes in the lattice [17].

A commonly used method to produce nanosized oxide dispersed strengthened (ODS) tungsten powders is mechanical milling (MM) or mechanical alloying (MA). However, the oxide nanoparticles still tend to be agglomerated to some extent because of the high surface energies introduced, typically with submicron or micron size [18,19]. The milling processing also results in contamination by the wear of the milling equipment and media. Nanostructure tungsten based powders can also be made by bottom-up methods starting from the atomic or molecular level. The wet-chemical process has been proved to be effective in fabricating complex nanostructured materials, and has shown high promise for the preparation of nanomaterials with precise composition with very high purity and homogeneity [18–22]. The method is also suited for the fabrication of tungsten based composites. A major challenge in the sintering of nanopowders is to achieve full densification while preserving the nanoscale. One such recent technological innovation is the use of spark plasma sintering (SPS), which is a pressure-assisted sintering that utilizes a large pulsed DC current (1000–5000 A) to heat the compacts and molds. SPS process provides fast heating rate (up to 1000 °C/min) and

---

* Corresponding authors at: School of Materials Science and Engineering, Hefei University of Technology, Hefei 230009, China. Tel./fax: +86 551 62901012.
E-mail address: luolaima@126.com (L.-M. Luo).

short sintering time, and allows the consolidation of powder materials into dense fine-grained products at lower sintering temperature [23–25].

In this paper, we have developed a novel method for the synthesis of nano ODS-W powders, in which a precursor of tungsten and metal oxides is prepared by the reaction of tungsten and praseodymium salts in aqueous solution at room temperature. The obtained precursor is highly homogenous where the two components are mixed at the molecular level. The doped precursor was reduced in hydrogen atmosphere and the reduced powders were then sintered into $W–Pr_2O_3$ composites by SPS to demonstrate their homogenous distribution and the sinterability of the as-synthesized Pr_2O_3/W powders. It is concluded that the powder could be consolidated to a uniform ultrafine bulk material with oxide particles dispersed both inside and at the boundaries of the tungsten grains.

2. Experimental procedure

2.1. Precursor synthesis, reduction and sintering

Ammonium paratungstate hydrate (APT, Aladdin) was suspended in an aqueous solution of praseodymium nitrate hexahydrate (Aladdin) to synthesize praseodymium doped tungsten precursors with praseodymium content corresponding to $W–1$ wt% Pr_2O_3. About 30 g of APT ($H_{42}N_{10}O_{42}W_{12}\cdot x H_2O$) and 0.56 g of praseodymium nitrate ($PrN_3O_9\cdot6H_2O$) were dissolved in sequence in 150 ml of deionized water under vigorous stirring at room temperature. The solution was filtered after 24 h reaction to ensure complete reaction between APT and Pr ions and the obtained powder was dried at 60 °C for 2 h. The powder was then calcined under nitrogen atmosphere at 450 °C for 1 h whereby the powder was transformed into oxide mixture. Next, the precursor was reduced by high purity hydrogen in a single-tube electrically heated furnace. The boat containing the precursor was placed in the central section of the furnace tube and heated to 800 °C at 5 °C/min in a gas flow, then maintained at that temperature for 6 h. After that, the sample was cooled to room temperature, still under a hydrogen flow. In a separate experiment, the as-received APT was reduced to pure tungsten powder under the same conditions.

The consolidation of the samples was carried out through SPS (FCT Group, SE-607, Germany) technique. The temperature profile of the sintering program in this study was illustrated in Fig. 1. Under the action of a uniaxial pressure increased slowly to 43.3 MPa, the powders were heated by pulse current to 450 °C. Then under the constant pressure of 43.3 MPa, the powders were
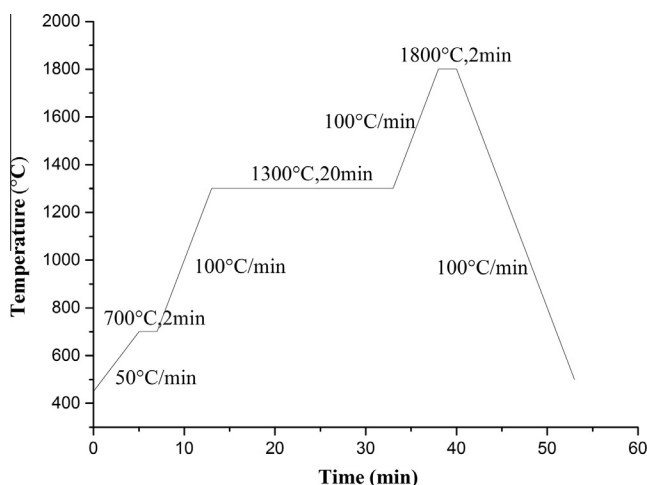
heated to 700 °C with a heating rate of 50 °C/min. The powders were held at 700 °C for 2 min and the pressure was increased from 43.3 MPa to 57 MPa at the same time. All these above sintering processes were conducted in vacuum. Then a flowing gas mixture of argon and hydrogen atmosphere was used for the following sintering processes. The samples were heated to 1300 °C with a heating rate of 100 °C/min and held at 1300 °C for 20 min. Subsequently, the samples were heated to 1800 °C at a heating rate of about 100 °C/min, and after 2 min soaking they were cooled down to room temperature with a cooling rate of 100 °C/min. The size of the sintered samples was about 20 mm in diameter and 2.0–3.0 mm in thickness. Densities measurements of sintered samples were conducted by the Archimedes method. The relative densities (RD) were calculated using theoretical densities of tungsten and Pr_2O_3 as 19.3 g/cm^3 and 6.85 g/cm^3 respectively. Polished sintered samples were subjected to Vickers microhardness testing under 200 g loads and a dwell time of 20 s at room temperature. The Vickers microhardness was calculated as a mean of ten measurements.

2.2. Microstructure characterization

The microstructure and particle morphology of the precursor and reduced powders were studied by field emission scanning electron microscope (FE-SEM, SU8020) and energy dispersive X-ray spectrometer (EDS) analysis detectors. X-Ray diffraction (D/MAX 2500V) was employed for the characterization of the prepared materials. The morphologies of the SPS-sintered bulk tungsten materials were characterized by FE-SEM and transmission electron microscopy (TEM, JEF-2100F). Energy-dispersive X-ray spectroscopy (EDX) analytical system installed on TEM was used for elemental analysis. Grain sizes were measured from Secondary Electrons (SE) images of fractured samples. TEM samples were sectioned with a diamond saw and mechanically ground to about 50 μm thick circular discs with 3 mm in diameter. The samples were dimpled to about 20 μm and then ion thinned with Ar$^+$ ions until perforation occurred.

2.3. Tensile property test

Tensile testing was performed using Instron testing machine (Instron 5967). The tensile test specimens are dog-bone shaped with an overall length of 16 mm, a gauge length of 5 mm and an effective cross section of 4×0.75 mm as shown in Fig. 2. The behaviors of BCC metals show a strong dependence of the yield stress on the strain rate and temperature. Moreover, the yield stress of W is strongly temperature dependent, and one expects a strong rate dependence of the flow stress. Therefore, the tests were performed with strain control and deformation speed of 0.05 mm/min was applied. For the alignment of the specimen, a preloading of 5 N was applied.

2.4. Thermophysical properties test

Thermal conductivity test was performed using laserflash thermal analyzer (LFA 457, Germany). Measurements of thermal diffusivity (α) of the materials from room temperature to 800 °C
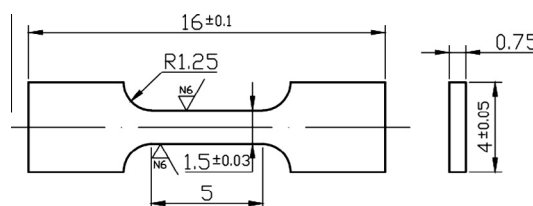

Fig. 1. Temperature profile of SPS process for the pure tungsten and $W–Pr_2O_3$ composites.

Fig. 2. Drawing of the tensile specimen with dimensions.

were carried out by using the laser-flash technique with disk samples of 6 mm diameter and 2–3 mm thickness. Thermal conductivity (κ) was calculated from the relationship: $\kappa = Cp\rho\alpha$, where Cp is the specific heat capacity at constant pressure and ρ is the material's density. The Cp parameter was measured with a heat-compensation-type differential scanning calorimeter using sapphire as a reference material. The density was measured by the Archimedes water-immersion method at room temperature.

3. Results and discussion

3.1. Synthesized precursor

The precursor synthesis started by the suspension of APT powder in an aqueous solution of praseodymium nitrate at room temperature. When the reaction was carried out in the presence of $Pr(NO_3)_3$ (aq), Pr^{3+} ions were randomly incorporated inside or adsorbed on the surface of the tungsten oxide nanoparticles, in either case, resulting in the formation of a very uniform mixture of praseodymium and tungsten ions. The synthesized powder precursors were analyzed by FE-SEM. As can be seen in Fig. 3, the precursor powders are caked together. Pr doped–W precursor powder was rather similar to starting APT powder in morphology, and consists of agglomerates with a size distribution of 10–20 μm. HR-SEM Fig. 3b revealed that Pr containing oxide products were found on the surface of the APT particles, having 2-dimensional plate-like morphology. The qualitative EDS analysis from such plate-like particles showed the presence of three elements, Pr, O and W, indicating that these particles were newly formed as a result of the reaction in solution.

3.2. Reduced powder

Reduction processing of the precursor in nitrogen followed by hydrogen resulted in the formation of a powder consisting of particles with two different morphologies: (i) larger particles, <2 μm, with a polygonal morphology, and (ii) finer particles (100–150 nm) in cubic shapes, as shown in Fig. 4a and b. These finer particles were clustered into agglomerates. Qualitatively Pr and oxygen were confirmed in these particles by EDS analysis at 15 kV. Tungsten was also detected together with Pr and oxygen, due to comparatively a large interaction volume in relation to grain size. The compositional analysis from reduced powder was corresponding to W–1 wt% Pr_2O_3. Fig. 5a is the XRD pattern of reduced powder. All the diffraction peaks can be indexed undisputedly to be the standard body centered cubic structure pure tungsten (JCPDS#04-0806). Strong diffraction peak intensity and narrow diffraction peak width reveal a good crystal structure. No peak of any other phases or impurities was observed from the patterns, demonstrating that tungsten crystalline with high purity could be obtained by the current synthetic route. No Pr_2O_3 peak was detected in the XRD pattern of the reduced product, which is the evidence of the low proportion of Pr_2O_3.
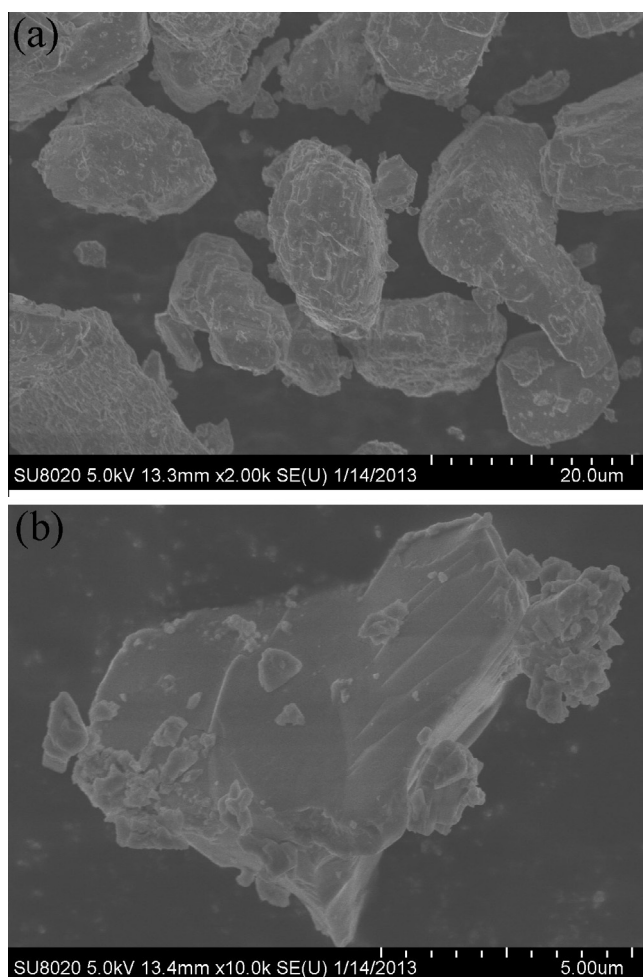

Fig. 3. SEM micrograph of (a) low magnification image of precursor powder, (b) high magnification image of Pr containing plate like particles in the precursor.
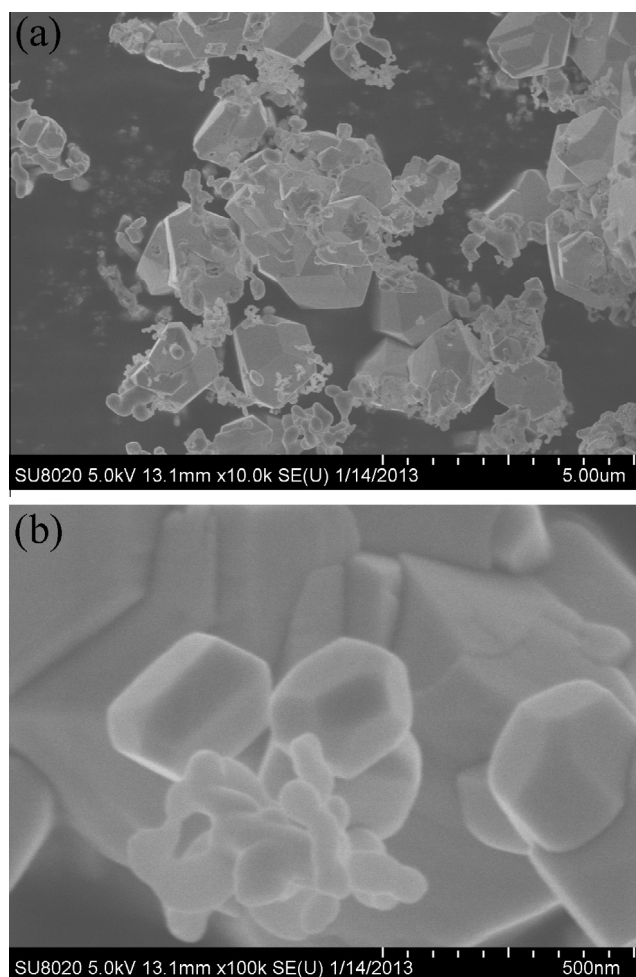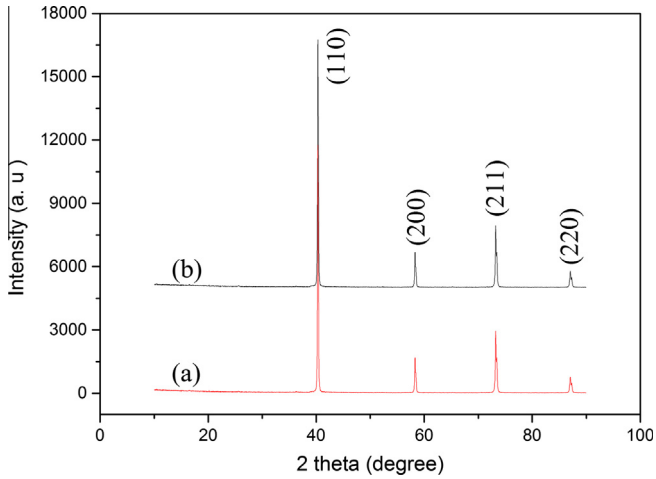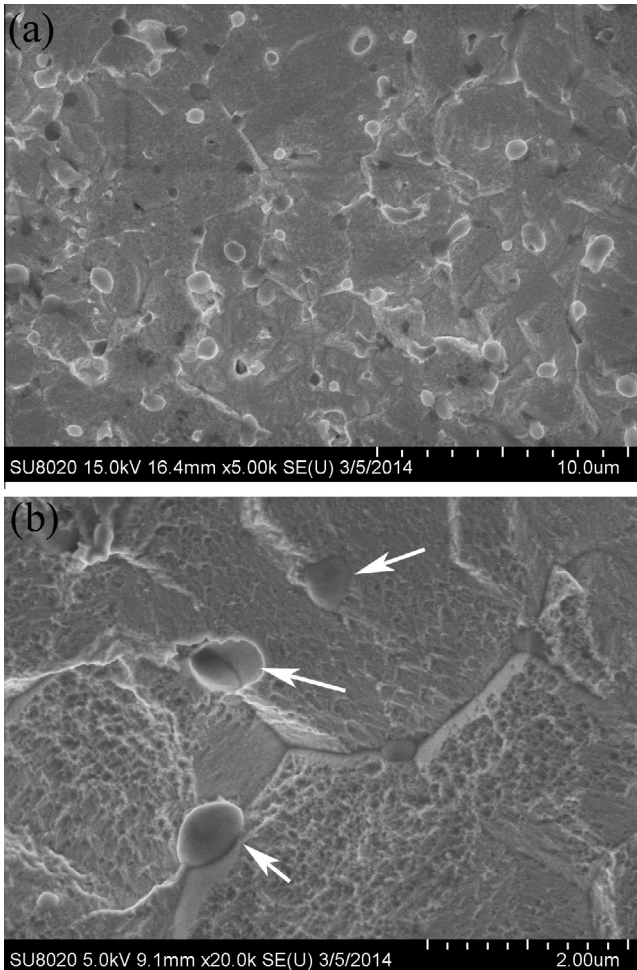

Fig. 4. SEM micrograph of (a) precursor after reduction, (b) high resolution image of finer particles (100–150 nm) of cubic shape.
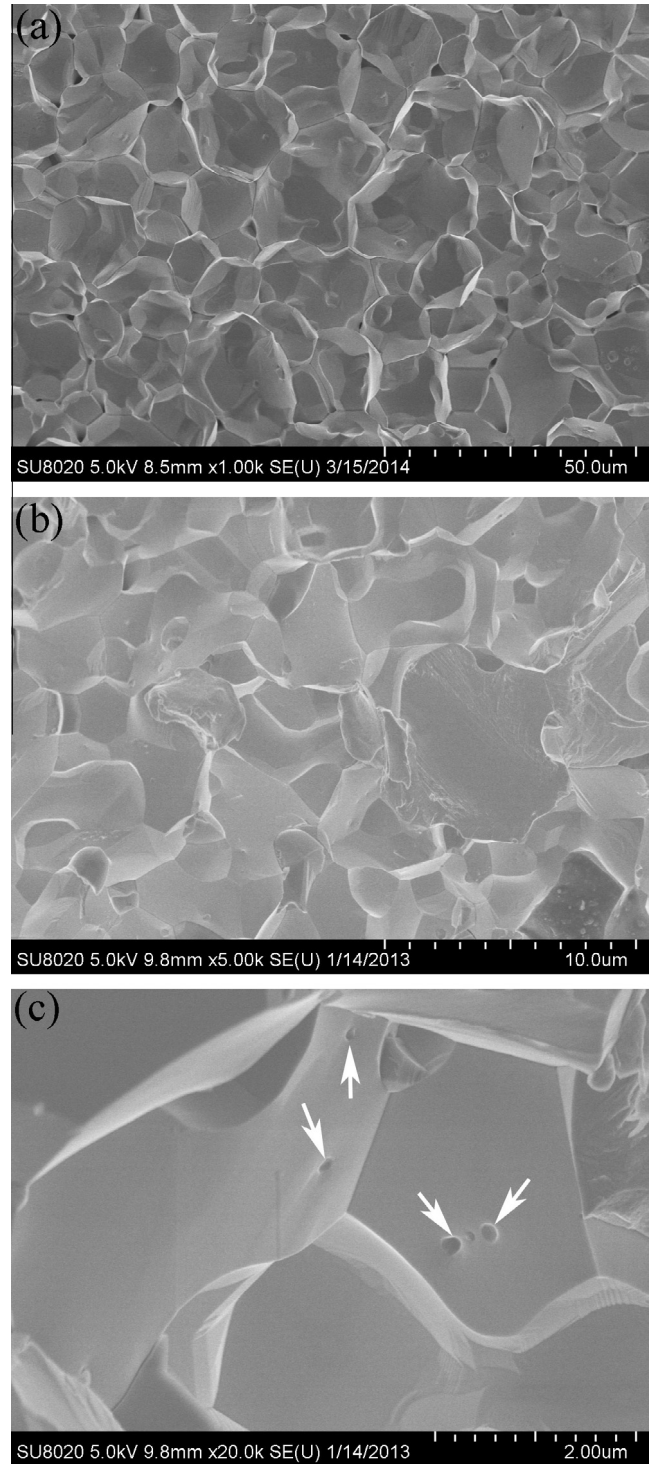
Fig. 5. XRD patterns of (a) reduced powder, (b) W–Pr$_2$O$_3$ composites sintered by SPS.

Fig. 6. (a) Low magnification SEM image showing the porosity and oxide distribution, (b) high resolution image showing oxide particles at the tungsten grain boundaries as well as within the grains.

Fig. 7. SEM micrographs of fracture surface for: (a) Pure W, (b) W–1 wt% Pr$_2$O$_3$ and (c) high resolution image showing oxide particles and empty sites.

3.3. SPS sintering

The reduced powders were pressed into a graphite die and sintered into discs of 20 mm in diameter and around 2.5 mm in height by SPS technique. As shown in Fig. 6a, low magnification SEM image shows the porosity and oxide distribution in the sintered sample. Fig. 6a reveals the nearly fully dense surface of SPS-sintered tungsten, in agreement with the high relative density of 98.3. It is obvious from the HR-SEM images (Fig. 6b) that the oxide particles are dispersed at the tungsten grain boundaries as well as within the grains. XRD analyze (Fig. 5b) exhibits that no peak of any other phases or impurities was observed from the patterns and the XRD pattern of the sintered material agrees with the patterns produced for the powders, indicating that no major phase change occurred during the SPS process. The sintered samples has a narrow Vickers microhardness distribution with a mean

Table 1
Density, grain size, Vickers micro-hardness of pure W and W–1 wt% Pr_2O_3 samples sintered by SPS.
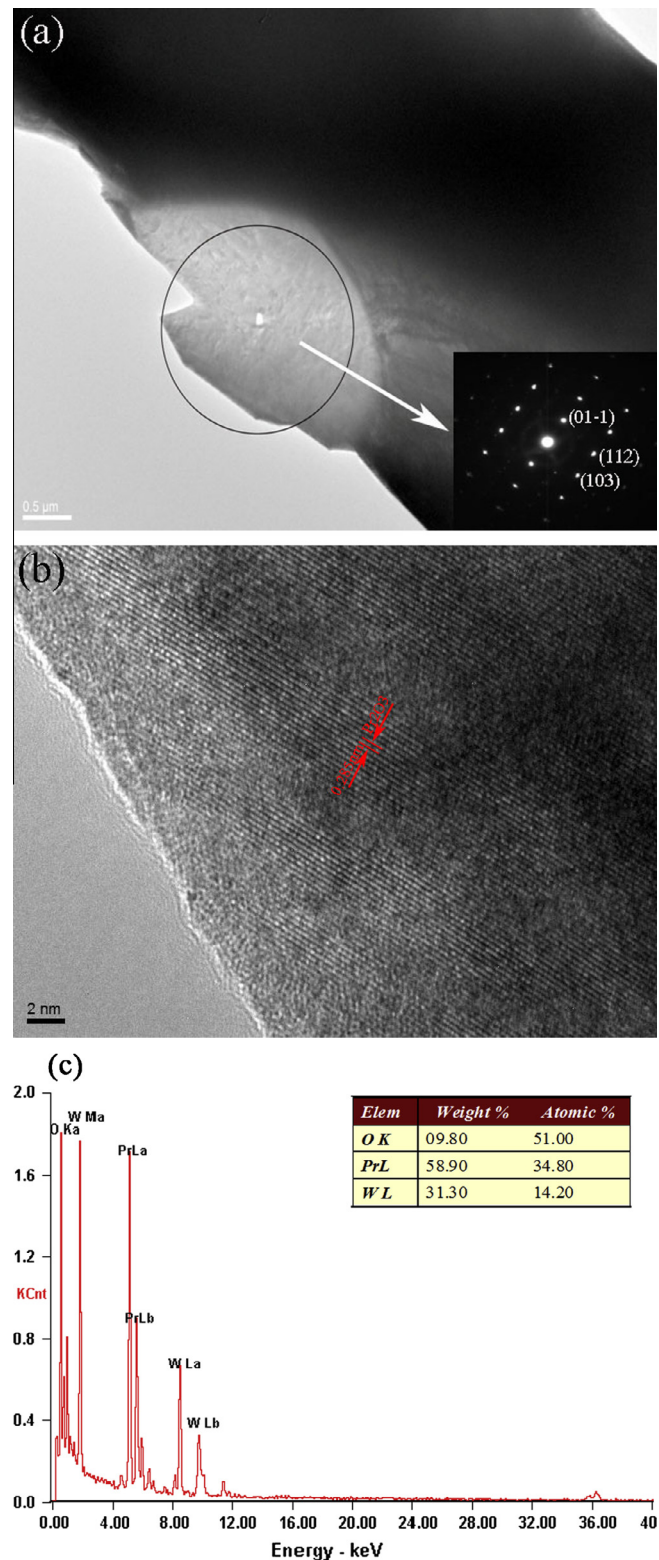
Materials	Density (g/cm^3)	Relative density (%)	Grain size (μm)	HV$_{200g}$
W	18.5	95.8	10	270
W–1 wt%Pr_2O_3	18.7	98.3	4	377
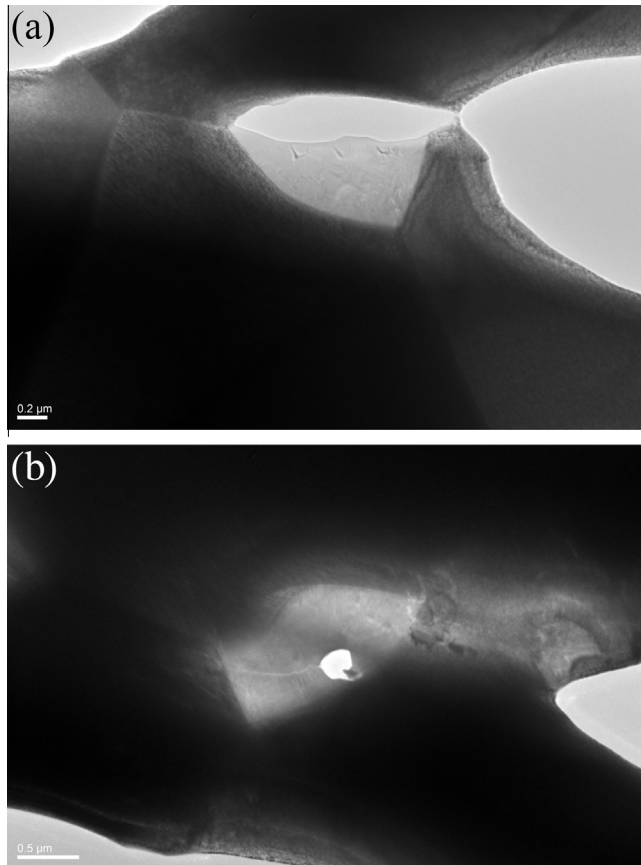
Fig. 8. TEM micrographs of dispersed particles in W–1 wt% Pr_2O_3 composites, (a) particle bound to the grain boundary and (b) particles dispersed in the matrix of tungsten.

Fig. 9. (a) TEM image of a spherical particle and insets of SAED pattern of oxide phase, (b) HRTEM image of the selected region in (a) and (c) EDX spectra and inset table with atomic ratio.

value about HV = 377.2 at 200 g, demonstrating the uniform structure of the sample from as-prepared powders. The highly uniform distribution of oxides in the sintered bulk material is an indication of the homogeneous mixing of W and Pr during the synthesis of the precursor. The new method offers considerably higher control of the chemical and microstructural uniformity than generally achieved by milling of powders [18].

The fracture surface of W–1 wt% Pr_2O_3 samples was presented in Fig. 7b and c, where the results of pure tungsten were shown for comparison (Fig. 7a). The fresh fracture surface was obtained by breaking the specimen after tensile test at room temperature. W-Pr_2O_3 exhibited lower porosity as compared to pure. Fig. 7a showed the average grain size of pure tungsten were 10 μm. The average grain size of sintered W–1 wt% Pr_2O_3 is about 4 μm, which are much smaller than that of pure tungsten, as listed in Table 1. These results demonstrated that oxide particles such as Pr_2O_3 were effective in hindering the grain growth of tungsten in the sintering process. More careful analysis of Fig. 7 reveals that the fracture surface is typical intergranular failure, indicating that these samples are brittle at room temperature. High resolution image (Fig. 7c) shows that empty sites of similar size and shape to the oxide particles were observed at the tungsten grains' facets. We consider

that during fracturing, some oxide particles were detached from the opposite fractured surface. Some empty sites were also found inside the tungsten grains, indicating that some grains have experienced a transgranular fracture.

In order to characterize the dispersion of the Pr_2O_3 dispersoid particles, TEM analysis was carried out. As showed in Fig. 8, the
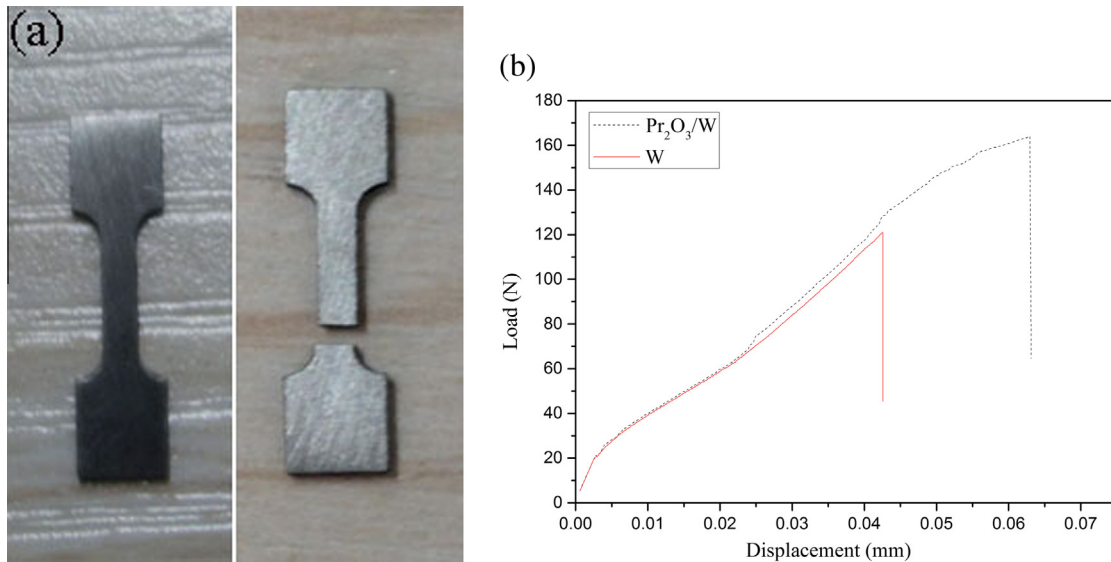
Fig. 10. (a) Tensile test specimen showing a brittle failure, (b) comparison of the load–displacement curves deduced from the tensile test of pure W and W–1 wt% Pr_2O_3 composite.

TEM images of W–1 wt% Pr_2O_3 composites reveal that parts of particles are tightly bound to the grain boundary (Fig. 8a) of tungsten and parts of them are homogeneously dispersed in the tungsten matrix (Fig. 8b). The inclusion of oxide particles most likely takes place during the formation of the previously described cube-shaped tungsten particles. The oxide particles may act as nucleation sites during the reduction of tungsten oxide, resulting in the growth of cubic tungsten particles around an oxide core. To further clarify the phase of such particles, the selected area electron diffraction pattern (SAEDP) and a HRTEM image of a particle with diameter of about 1 μm in a sample of W–1 wt% Pr_2O_3 were analyzed, as shown in Fig. 9a and in the inset and Fig. 9b, respectively. The SAEDP reveals that the particle is crystalline and exhibits a trigonal structure. In Fig. 9c, the EDX analysis from the particle revealed that the phase consists of only W, Pr and O with an approximate atomic ratio of 14:35:51. W was also detected together with Pr and oxygen, due to the matrix surrounding the particle. Combined with the above analysis, it could be concluded that the particle is the trigonal Pr_2O_3. The homogeneous dispersion of oxide particles in tungsten could pin dislocations and grains boundaries, and thus inhibit the grain growth, enhance the high temperature strength, and improve the recrystallization temperature.

3.4. Tensile test

Tensile testing was performed using Instron testing machine at room temperature with a loading rate of 0.05 mm/min. Fig. 10b compared the load–displacement curves deduced from the tensile test of pure W and W–1 wt% Pr_2O_3 composites. All specimens failed by a brittle manner at room temperature without an apparent plastic deformation and the fracture appearance were smooth and bright, as shown in Fig. 10a. Obviously, the tensile strength of Pr_2O_3/W was much higher than that of pure W, indicating that dispersing particles in the grain interior and at the grain boundaries can pin dislocations and grain boundaries, which is an effective approach to increase the tensile strength. The curve of Pr_2O_3/W specimen shows a rapid increase at the initial stage and a slow increase in the next stage. It may because during the tensile process, the crack propagates along the grain boundaries, and then propagates to the inside. The oxide particles in the grain hinder the fracture, thereby slowing the rate of fracture.
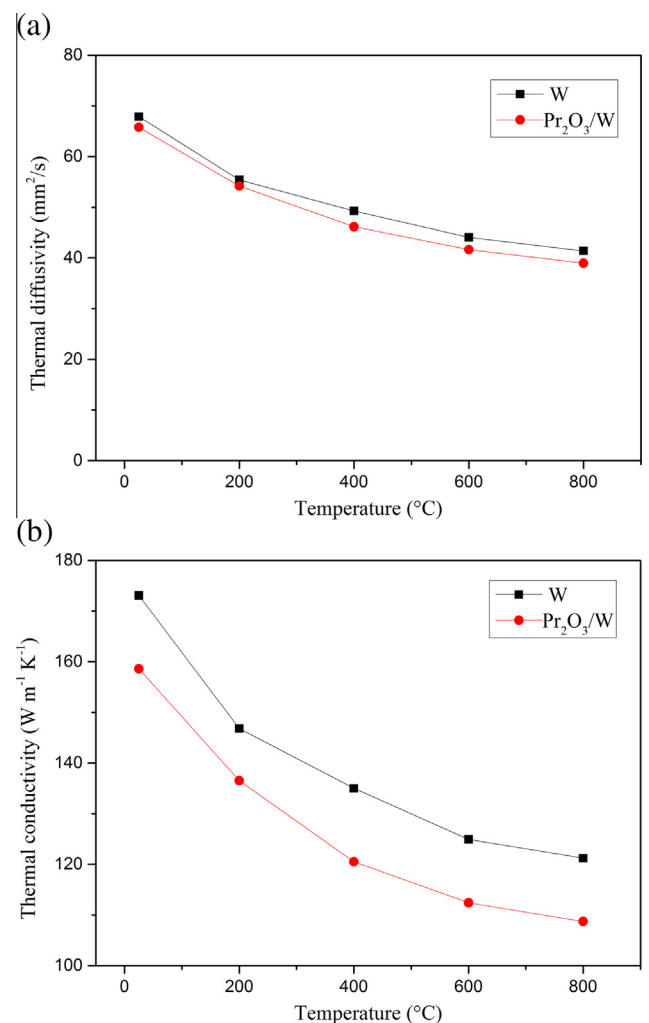
Fig. 11. (a) Thermal diffusivities and (b) thermal conductivities versus temperature of pure W and W–1 wt% Pr_2O_3 composite.

3.5. Thermophysical properties

The thermal diffusivities and thermal conductivities of the Pr_2O_3/W composites from 25 °C to 800 °C are shown in Fig. 11a and b, respectively. The thermal diffusivity of pure W drastically decreased from 67.9 mm^2/s at 25 °C to 41.4 mm^2/s at 800 °C, and that of the Pr_2O_3/W composites decreased with the same trend as the temperature increased in the testing temperature range, although the diffusivities of the composites were lower compared with that of pure W. Both the thermal conductivity of pure W and W–1 wt% Pr_2O_3 composites decreased with increasing temperatures. Thermal conduction includes electron conduction and phonon conduction, and electron conduction is the main way for metals because the thermal conductivity, κ_e of the electron conduction is much higher than that of the phonon conduction. κ_e is a decreasing function of temperature for monolithic tungsten [26]. Therefore, the thermal conductivity of monolithic tungsten decreases with increasing temperature, which is in accordance with the measured results. The conductivity of the Pr_2O_3/W composites is mainly determined by the thermal conductivity of the tungsten matrix and oxide particles reinforcement, and the particle volume fraction and particle distribution status in the tungsten matrix. Due to the relatively low volume fraction and the random distribution (relatively uniform distribution) of Pr_2O_3 particles, the particles cannot form continuous paths through the matrix, thus the thermal conductivity is mainly controlled by the matrix. With increasing temperature, the thermal conductivity of Pr_2O_3/W composites decreased.

4. Conclusions

Oxide Dispersion-Strengthened (ODS) materials W–1 wt% Pr_2O_3, doped with highly uniform Pr_2O_3 was successfully synthesized by a novel wet chemical method. The powders were prepared in two steps, starting with the synthesis of a precursor from APT and praseodymium nitrate from aqueous solution at room temperature for 24 h and then followed by reduction in hydrogen atmosphere to a composite powder. Pr_2O_3/W composites are successfully sintered by SPS technique in much shorter time than those in conventional sintering methods which avoided substantial grain growth. The SEM images demonstrated that Pr_2O_3 particles are homogeneously distributed in the tungsten matrix. The grain size, relative density and the Vicker hardness $HV_{0.2}$ of the bulk samples fabricated by SPS sintering were 4 μm, 98.3% and 377.2, respectively. The tensile strength values of Pr_2O_3/W samples were higher than those of pure W samples. As the temperature rises from 25 to 800 °C, the conductivity of pure W and W–1 wt% Pr_2O_3 composites decreased with the same trend. However, it is worth noting that the thermal conductivity of both samples was above 150 W/m K at room temperature. Our results demonstrate that wet chemical process is a good method for preparing ODS–W composite powder, and SPS sintering method is an effective technique for fabricating dense tungsten with fine microstructure.

References

[1] D. lee, M.A. Umer, H.J. Ryu, S.H. Hong, Int. J. Refract. Met. H 43 (2014) 89.
[2] A. Genç, S. Coskun, M.L. Öveçoğlu, J. Alloy. Compd. 497 (2010) 80.
[3] R. Liu, Y. Zhou, T. Hao, T. Zhang, X.P. Wang, C.S. Liu, Q.F. Fang, J. Nucl. Mater. 424 (2012) 171.
[4] S. Matsuo, H. Kurishita, H. Arakawa, T. Ogawa, A. Hasegawa, K. Abe, H. Arakawa, S. Matsuo, T. Takida, K. Takebe, M. Kawai, N. Yoshida, Mater. Sci. Eng., A 492 (2008) 475.
[5] Z.C. Chen, M.L. Zhou, T.Y. Zuo, Scr. Mater. 43 (2000) 291.
[6] Y. Ma, J.J. Zhang, W.S. Liu, P. Yue, B. Huang, Int. J. Refract. Met. H. 42 (2014) 71.
[7] W. Setyawan, R.J. Kurtz, Scr. Mater. 66 (2012) 558.
[8] J. Reiser, M. Rieth, A. Möslang, B. Dafferner, A. Hoffmann, X. Yi, D.E.J. Armstrong, J. Nucl. Mater. 434 (2013) 357.
[9] M. Kajioka, T. Sakamoto, K. Nakai, S. Kobayashi, H. Kurishita, S. Matsuo, H. Arakawa, J. Nucl. Mater. 417 (2011) 512.
[10] H. Kurishita, S. Matsuo, H. Arakawa, S. Matsuo, H. Arakawa, T. Sakamoto, S. Kobayashi, K. Nakai, T. Takida, M. Kato, M. Kawai, N. Yoshida, J. Nucl. Mater. 398 (2010) 87.
[11] D. Lee, M.A. Umer, H.J. Ryu, S.H. Hong, Int. J. Refract. Met. Hard Mater. 44 (2014) 49.
[12] K. Cui, Y.Z. Shen, J. Yu, B. Ji, Int. J. Refract. Met. Hard Mater. 41 (2013) 143.
[13] H. Kurishita, S. Kobayashi, K. Nakai, T. Ogawa, A. Hasegawa, K. Abe, H. Arakawa, S. Matsuo, T. Takida, K. Takebe, M. Kawai, N. Yoshida, J. Nucl. Mater. 377 (2008) 34.
[14] M. Roosta, H. Baharvandi, Int. J. Refract. Met. Hard Mater. 28 (2010) 587.
[15] M.C. Teague, G.E. Hilmas, W.G. Fahrenholtz, J. Am. Ceram. Soc. 92 (2009) 1966.
[16] T.Q. Zhang, Y.J. Wang, Y. Zhou, G.M. Song, Int. J. Refract. Met. Hard Mater. 28 (2010) 498.
[17] G. Liu, G.J. Zhang, F. Jiang, X.D. Ding, Y.J. Sun, J. Sun, E. Ma, Nat. Mater. 12 (2013) 344.
[18] M.A. Yar, S. Wahlberg, H. Bergqvist, H.G. Salem, M. Johnsson, M. Muhammed, J. Mater. Chem. 22 (2012) 12622.
[19] M. Xia, Q.Z. Yan, L. Xu, H.Y. Guo, L.X. Zhu, C.C. Ge, J. Nucl. Mater. 434 (2013) 85.
[20] M. Xia, Q.Z. Yan, L. Xu, L.X. Zhu, H.Y. Guo, C.C. Ge, J. Nucl. Mater. 430 (2012) 216.
[21] R.G. Chaudhuri, S. Paria, Chem. Rev. 112 (2012) 2373.
[22] M.A. Yar, S. Wahlberg, H. Bergqvist, H.G. Salem, M. Johnsson, M. Muhammed, J. Nucl. Mater. 408 (2011) 129.
[23] Z.M. Xie, R. Liu, Q.F. Fang, Y. Zhou, X.P. Wang, C.S. Liu, J. Nucl. Mater. 444 (2014) 175.
[24] L. Ding, D.P. Xiang, Y.Y. Li, C. Li, J.B. Li, Int. J. Refract. Met. Hard Mater. 33 (2012) 65.
[25] M.A. Yar, S. Wahlberg, H. Bergqvist, H.G. Salem, M. Johnsson, M. Muhammed, J. Nucl. Mater. 412 (2011) 227.
[26] G.M. Song, Y.J. Wang, Y. Zhou, Int. J. Refract. Met. Hard Mater. 21 (2003) 1.